

See discussions, stats, and author profiles for this publication at: <https://www.researchgate.net/publication/259113784>

Investigation of nanolevel molecular packing and its role in thermo-mechanical properties of PVA-fMWCNT composites: Positron annihilation and small angle X-ray scattering studies

ARTICLE *in* PHYSICAL CHEMISTRY CHEMICAL PHYSICS · DECEMBER 2013

Impact Factor: 4.49 · DOI: 10.1039/c3cp54054e · Source: PubMed

CITATIONS

6

READS

82

7 AUTHORS, INCLUDING:



S. K. Sharma

Bhabha Atomic Research Centre

53 PUBLICATIONS 162 CITATIONS

SEE PROFILE



Jyoti Prakash

Bhabha Atomic Research Centre

35 PUBLICATIONS 44 CITATIONS

SEE PROFILE



Jitendra Bahadur

Bhabha Atomic Research Centre

61 PUBLICATIONS 358 CITATIONS

SEE PROFILE



Shamsuddin Mazumder

Institute of Advanced Networking Technolo...

163 PUBLICATIONS 1,924 CITATIONS

SEE PROFILE

Cite this: DOI: 10.1039/c3cp54054e

Investigation of nanolevel molecular packing and its role in thermo-mechanical properties of PVA–fMWCNT composites: positron annihilation and small angle X-ray scattering studies

S. K. Sharma,^a J. Prakash,^b J. Bahadur,^c K. Sudarshan,^a P. Maheshwari,^a
S. Mazumder^c and P. K. Pujari^{*a}

Carbon based nanofillers have shown phenomenal improvements in thermo-mechanical properties of poly vinyl alcohol (PVA) based nanocomposites depending on their interaction with PVA molecules and dispersion in the polymer matrix. In the present study, PVA based nanocomposites with amino-functionalized multi-wall carbon nanotubes (fMWCNTs, 0.2, 0.4, 0.8 and 1.0 wt%) were prepared by a simple casting method from aqueous solution. The relative increase in Young's modulus with 0.4% fMWCNTs was observed to be comparable with that for PVA–nanodiamond composite films which have been shown to have higher strength compared to nanotube and graphene oxide based nanocomposites. In order to investigate the nanolevel molecular packing (sub-nano level free volumes and nano level lamellar structure) and its role in thermal and mechanical properties, positron annihilation spectroscopy and small angle scattering have been used. The crystallinity and morphology of the samples were characterized using X-ray diffraction and scanning electron microscopy. The studies showed that interfacial interaction between PVA molecules and functionalities on the surface of fMWCNTs results in the formation of an ordered structure of PVA molecules which enhances load transfer between the PVA matrix and fMWCNTs leading to improved mechanical properties. The thermal properties of the composites were observed to be unaffected at the studied filler concentration.

Received 25th September 2013,
Accepted 5th November 2013

DOI: 10.1039/c3cp54054e

www.rsc.org/pccp

1. Introduction

Polymer nanocomposites based on carbon nanotubes (CNTs) have shown improved properties and potential applications due to hybridization of their unique characteristics and functions.^{1–9} CNTs are assumed to increase the performance of polymer nanocomposites mainly because of their very high Young's modulus and tensile strength.^{10–12} Out of the various types of CNTs, single wall carbon nanotubes (SWCNTs) are assumed to be the best reinforcing fillers because of their smaller size and highest Young's modulus. However, limited reports are available on the use of SWCNTs as fillers in nanocomposites because of the complicated purification process and high cost for large scale production. On the other hand, multi-wall carbon nanotubes (MWCNTs) are grown on a larger scale using a chemical vapour deposition (CVD) method in a cost effective manner

which can provide better mechanical properties under specific conditions.¹³ MWCNTs have been extensively used for the preparation of polymer composites but limited enhancement in the mechanical properties has been observed. The limited enhancement has been attributed to different reasons. The main reasons are the dispersion of nanotubes in the polymer matrix, load transfer between polymer molecules and nanotubes, structural defects in the nanotubes and purity/quality of the nanotubes. Among these, load transfer between CNTs and polymer molecules can be enhanced by improving the interaction between CNTs and polymer molecules. One promising way to improve the interaction between CNTs and polymer molecules is functionalization of CNTs with organic functional groups which can interact with polymer molecules through hydrogen bonding or covalent bonds. The improved interfacial interaction also results in fine dispersion of CNTs even at higher loading.^{5,7} The disadvantage associated with the functionalization of CNTs is that it introduces defects in the CNT structure and deteriorates their mechanical strength. However, nanocomposites based on functionalized MWCNTs (fMWCNTs) are expected to provide improved mechanical properties compared to those based on pristine MWCNTs.

^a Radiochemistry Division, Bhabha Atomic Research Centre, Mumbai – 400085, India. E-mail: pujari@barc.gov.in

^b Materials Group, Bhabha Atomic Research Centre, Mumbai – 400085, India

^c Solid State Physics Division, Bhabha Atomic Research Centre, Mumbai – 400085, India

In general, evolved properties of the polymer nanocomposites are ascribed to different types of interfacial interactions between polymer molecules and CNTs. The interaction between polymer molecules and CNTs modifies the properties of the nanostructure, viz. (i) free volume nanohole size, density and size distribution and (ii) ordering of polymer molecules at the nanotube surface. These changes have direct correlation to various properties namely thermo-mechanical, electrical, dielectric, filtration, etc. Thus, the characterization of nanostructure of polymer composites with varying interfacial interaction is required to understand the role of interfacial interaction in both evolved nanostructure and properties of polymer composites. Positron annihilation lifetime spectroscopy (PALS) and small angle X-ray scattering (SAXS) are the best techniques to characterize the structure of polymer composites at the sub-nano and nano level. PALS provides information about the sub-nano level free volume size, density and size distribution in the polymer nanocomposites.^{14–19} In polymer nanocomposites, a fraction of positrons after thermalization form a quasi bound state, positronium (Ps), with an electron. The positronium can occur as a singlet spin state, *para*-positronium (*p*-Ps), or as a triplet spin state, *ortho*-positronium (*o*-Ps), with a relative abundance of 1 : 3. The intrinsic lifetimes of *p*-Ps and *o*-Ps are 125 ps and 142 ns, respectively. In polymer nanocomposites, Ps may annihilate with an electron other than its bound partner and having opposite spin (*pick-off* annihilation). As a result, the *o*-Ps lifetime reduces from 142 ns to 1–10 ns depending on the frequency of collision with the surrounding atoms. The *o*-Ps *pick-off* lifetime, τ_3 , in a polymer is correlated with the radius of free volume nanoholes using the Tao–Eldrup equation^{20,21}

$$\tau_3 = \frac{1}{2} \left[1 - \frac{R}{R + \Delta R} + \frac{1}{2\pi} \sin \left(\frac{2\pi R}{R + \Delta R} \right) \right]^{-1} \quad (1)$$

where $\Delta R = 0.166$ nm is an empirical parameter. The *o*-Ps intensity, I_3 , is used to obtain the fractional free volume, and a distribution over *o*-Ps lifetime provides free volume size distribution in the polymer nanocomposites. Recently, we have shown that positron and positronium are efficiently trapped at the nanoholes available at the interfaces which enables the characterization of the evolved nanostructure of polymer composites.^{18,19}

Poly vinyl alcohol (PVA), owing to its hydroxyl group, is the most suitable polymer for making polymer nanocomposites based on CNTs functionalized with hydrophilic functional groups. PVA has immense applications in fuel cells, coating materials, adhesives, drug delivery systems and functional membranes due to its unique characteristics such as water solubility, biocompatibility, non-toxicity and the presence of a hydroxyl-rich surface.² When nanofillers are distributed in PVA having different types of interfacial interactions at the molecular level, remarkable changes in properties such as mechanical, thermal and electrical properties have been reported.^{1–9,22–25} In the case of nanofillers modified with hydrophilic groups, hydrogen bonding between nanofillers and hydroxyl groups of PVA is shown to be responsible for these remarkable changes in

the properties. Hydrogen bonding helps in improving the dispersion of nanofillers providing a high surface area for an efficient load transfer. In addition to the mentioned effects, hydrogen bonding between nanofillers and polymer molecules is also expected to change the nanostructure of the polymer matrix. Thus, it is important to understand the evolved nanostructure of the composite along with the evolved properties.

In the present study, we have characterized the nanostructure of PVA-*f*MWCNT composites using positron annihilation spectroscopy (sub-nm level) and small angle X-ray scattering (nm level). MWCNTs functionalized with amino ($-\text{NH}_2$) groups have been used as nanofillers for the preparation of nanocomposites. PALS has been employed for the investigation of average size, density and size distribution of free volume nanoholes as a function of *f*MWCNT loading. Positron coincidence Doppler broadening (CDB) measurements have been carried out to investigate the change in the chemical surroundings of positron annihilation sites in the nanocomposites. Small angle X-ray scattering has been employed to investigate the changes in PVA structure on a larger scale (>1 nm) as a function of *f*MWCNT loading. The changes in nanostructure have been correlated with thermal and mechanical properties of the nanocomposites.

2. Experimental section

2.1. Sample preparation and characterization

PVA (average M.W. 89 000–98 000, more than 99% hydrolyzed) and ethylene diamine (M.W. 60.10) were used for the nanocomposite preparation. CNTs were prepared using a chemical vapour deposition (CVD) method and purified using a method reported by us elsewhere.¹⁸ In order to functionalize the MWCNTs with $-\text{NH}_2$ groups, ethylene diamine ($\text{NH}_2\text{--CH}_2\text{--CH}_2\text{--NH}_2$) was added to ethanol solvent and then the MWCNT dispersed ethanol solution was added to the solution under stirring. This solution was subjected to ultrasonic dispersion for 3.0 h. The MWCNT dispersed ethylene diamine solution was further heated at 80 °C for 6 h. After heat treatment the solvent was removed and the remaining black solid was dried in a vacuum oven for 12 h to obtain the final amino-modified MWCNTs. The ethylene diamine was adsorbed at the MWCNT surface either *via* physical adsorption or *via* formation of chemical bonds with $-\text{OH}$ and $-\text{COOH}$ groups available at the surface of MWCNTs due to the oxidative purification process. Thus produced *f*MWCNTs were dispersed in deionized (DI) water through ultrasonication to obtain a homogeneous dispersion. This solution has shown good stability of the MWCNT suspension for a longer duration. For the preparation of PVA-*f*MWCNTs, 5 g of PVA was dissolved in 20 ml of DI water at room temperature to form a polymer solution. The *f*MWCNTs were suspended in 10 ml of deionised water under ultrasonication at room temperature. The *f*MWCNT suspension was mixed with the polymer solution. Another 25 ml of DI water was used to rinse the beaker wall and remove the remaining *f*MWCNTs. The rinse solution was combined with the *f*MWCNT and PVA solution. The solution (total 55 ml) was heated to 90 °C under

ultrasonication and stirring for 6 h to obtain a homogeneous solution. The solution was cast on a glass Petri dish. A uniform thickness was obtained after drying in a vacuum at 60 °C for 8 h. Different percentages of *f*MWCNTs were with respect to PVA to obtain 0.2, 0.4, 0.8, and 1.0 wt% *f*MWCNT composites. These films were free from air bubbles and could be taken off easily from the glass surface. The thickness of the films was measured to be $100 \pm 10 \mu\text{m}$ using a digital micrometer.

The MWCNTs were characterized using a 2000FX JEOL transmission electron microscope. The *f*MWCNT–PVA composites were characterized using SEM–Camscan MV2300CT/100, UK. X-ray diffraction measurements using a Philips X pert pro XRD unit with Cu K α radiation were carried out to evaluate crystallinity of the composites. FTIR spectra of pure PVA, MWCNTs, *f*MWCNTs and *f*MWCNT–PVA composites were obtained using Vertex 80v (Bruker) under vacuum in diffuse reflection mode and a liquid nitrogen cooled MCT detector from 4000 to 400 cm $^{-1}$ at a resolution of 2 cm $^{-1}$.

2.2. Positron annihilation measurements

The nanocomposite films were heated at 40 °C for 4 h before carrying out the measurements to remove the absorbed water from the samples. The positron annihilation measurements were carried out at RT in the laboratory atmosphere. The positron source (^{22}Na , 10 μCi) was carrier free NaCl deposited between two 7 μm thick kapton foil. The positron source was sandwiched between two stacks of the nanocomposite films ensuring that all positrons annihilate within the sample. PALS measurements were carried out using a fast–fast coincidence setup coupled to plastic scintillation detectors. The time resolution of the lifetime spectrometer was 240 ps and the time calibration of MCA was 25 ps per channel. All the positron lifetime spectra contained $>10^6$ counts. Silicon single crystal was used as a reference material to estimate the fraction of positrons annihilating within the source (NaCl salt) and kapton foil. The routine CONTIN²⁸ was used to evaluate the average size, density as well as size distribution of free volume nanoholes.

For CDB measurements, two HPGe detectors (each having a resolution of 1.2 keV at 514 keV of ^{85}Sr) located at 180° relative to each other were used to record two annihilation photons E_1 and E_2 emitting from a single event. The difference ($\Delta E = E_1 - E_2$) and sum ($E_t = E_1 + E_2$) of the energies of two gamma rays are expressed as cP_L and $2m_0c^2 - E_B$, respectively. Here, P_L is the longitudinal component of the positron–electron momentum along the direction of the detector, c is the velocity of light, m_0 is the electron rest mass, and E_B is the electron binding energy. The Doppler shift $\Delta E = 1 \text{ keV}$ corresponds to $P_L = 1.956 \times 10^{-3} m_0 c$. Coincidence events were selected in the range of $2m_0c^2 - 3.0 \text{ keV} < E_t < 2m_0c^2 + 3.0 \text{ keV}$ for obtaining the annihilating electron momentum distribution. This resulted in a peak to background ratio of $>10^5$. The area under the Doppler broadened peak for all the samples was $>10^6$. The data were analyzed in the form of ratio curves by taking the ratio of the area normalized momentum distribution curve of the nanocomposites to pure PVA.

2.3. Small angle X-ray measurements (SAXS)

SAXS measurements were performed on the nanocomposite films after heating under the same condition as for positron annihilation measurements using a lab based SAXS setup having Cu K α source, and the diameter of the incident photon beam on the sample was 0.4 mm. The SAXS detector was mounted at a sample-to-detector distance of 1.07 m, corresponding to a q -range of 0.01–0.25 Å $^{-1}$. The magnitude of the scattering wave vector, q , was equal to $2\sin\theta/\lambda$, where 2θ is the scattering angle and $\lambda = 0.154 \text{ nm}$ the used wavelength.

2.4. Thermal and mechanical properties

Thermal gravimetric analysis (TGA) of MWCNTs, *f*MWCNTs and *f*MWCNT–PVA composites was carried out using a Netzsch thermobalance under an inert atmosphere at a heating rate of 10 K min $^{-1}$. Tensile properties of the samples dried under the same condition as for positron annihilation and SAXS measurements were determined using a tensile tester, Autograph AGS-1kND (Shimadzu Co.); the initial length of the specimen was 20 mm, and the extension rate was 2 mm min $^{-1}$. The number of tested specimens was more than five.

3. Results and discussion

3.1. *f*MWCNT characterization

The HRTEM bright field image of the synthesized CNTs is shown in Fig. 1. The size of the CNTs can be determined by measuring the distance between two dark lines observed in TEM overviews.²⁶ The image showed that the CNT length was of micrometer range and the average outer diameter measured from the images was $\sim 50\text{--}70 \text{ nm}$. The image (c) also confirmed that the synthesized CNTs are MWCNTs and non-alignment of the graphene layer indicated formation of defects in modified MWCNTs (after the oxidative purification process). The MWCNTs were functionalized using ethylene diamine to incorporate $-\text{NH}_2$ functions on their surface. The *f*MWCNTs were characterized using FTIR and TGA. The FTIR spectrum of MWCNTs (Fig. 2) shows the presence of $-\text{COOH}$ and $-\text{OH}$ groups ($-\text{C}=\text{O}$, 1713 cm $^{-1}$ and $-\text{OH}$, 3413 cm $^{-1}$) due to the oxidative process of purification of

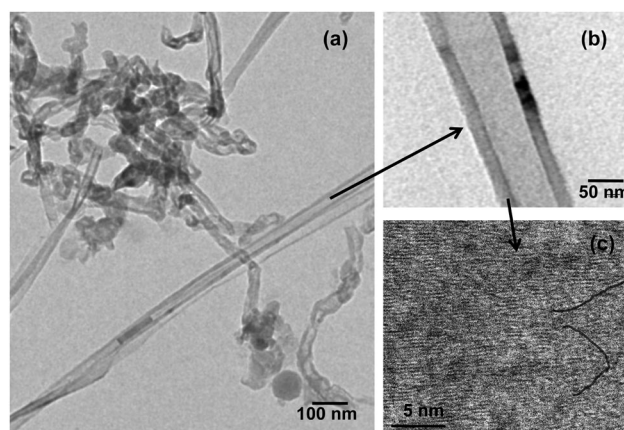


Fig. 1 HRTEM images of synthesized MWCNTs.

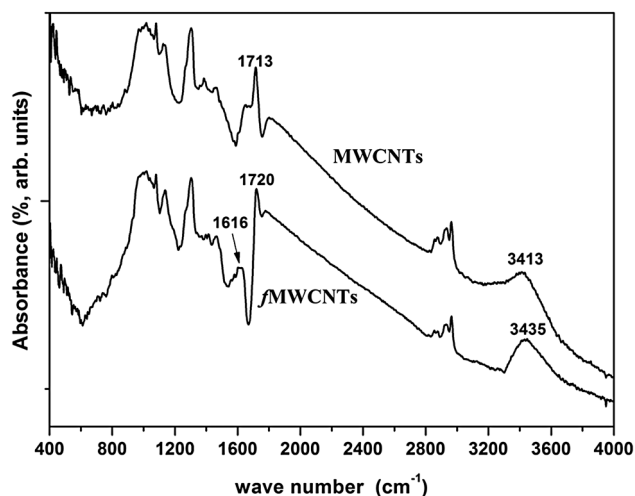


Fig. 2 FTIR spectra of MWCNTs and *f*MWCNTs.

MWCNTs. The presence of these groups on the MWCNT surface is well reported in the literature.²⁷ On reaction with ethylene diamine, the presence of peaks corresponding to N–H bending (1616 cm^{-1}) and stretching (3435 cm^{-1}) confirms the presence of --NH_2 groups on the MWCNT surface. The shifts observed in --C=O and --OH stretching (Fig. 2) indicate the reaction of ethylene diamine with --COOH and --OH functional groups present at the surface along with the physical adsorption of ethylene diamine molecules at the defected surface sites. This has been confirmed by TGA measurements as shown in Fig. 3. The derivatives of TGA curves of MWCNTs and *f*MWCNTs have been plotted as an inset in Fig. 3. In the case of MWCNTs, weight loss is observed in the temperature range of 350–450 K, indicating the disruption of functionalities (--COOH and --OH) produced due to the oxidative purification process. On the other hand, in the case of *f*MWCNTs, two weight loss processes are observed in the temperature range of 300–400 K and 450–650 K, indicating the

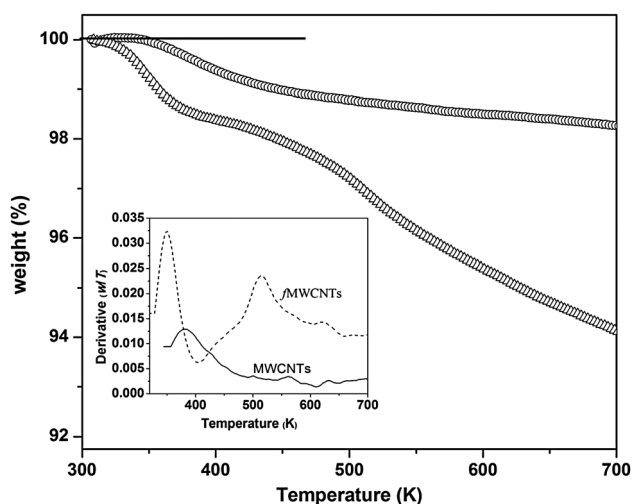


Fig. 3 TGA curves of MWCNTs (○) and *f*MWCNTs (Δ). The inset shows the derivative of TGA curves for MWCNTs (solid line) and *f*MWCNTs (dashed line).

disruption of physically adsorbed ethylene diamine and chemically bound ethylene diamine (to --COOH and --OH), respectively.

3.2. Nanocomposite characterization

Fig. 4 shows the optical images of PVA and the nanocomposite films indicating that all the films are homogeneous on a large scale. Fig. 5 shows the XRD pattern for pure PVA and the nanocomposite films. The characteristic diffraction peak for pure PVA is observed at $2\theta \sim 22^\circ$, and on incorporation of *f*MWCNTs, this peak becomes narrower indicating the change in crystallinity of PVA. No new peak was observed after the incorporation of *f*MWCNTs indicating fine dispersion of *f*MWCNTs in the PVA matrix. To evaluate the relative crystallinity, the broad diffraction peak was fitted to two Gaussian (narrow and broad) peaks corresponding to the crystalline and amorphous regions of PVA. The ratio of area of the fitted peaks (crystalline/amorphous) was calculated as relative crystallinity of PVA and the nanocomposites. It was observed that the relative crystallinity of all the nanocomposites was higher compared to that of pure PVA (16.5%). The increased crystallinity observed for

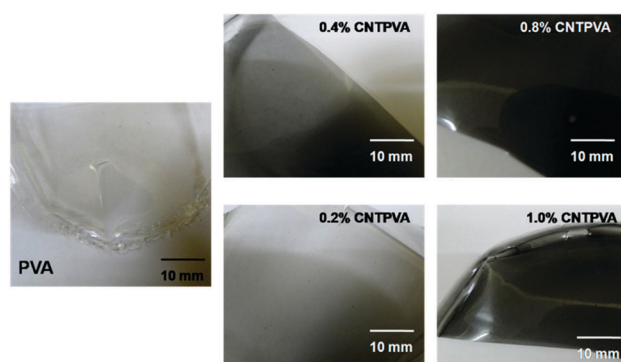


Fig. 4 Optical images of pure PVA and nanocomposite films.

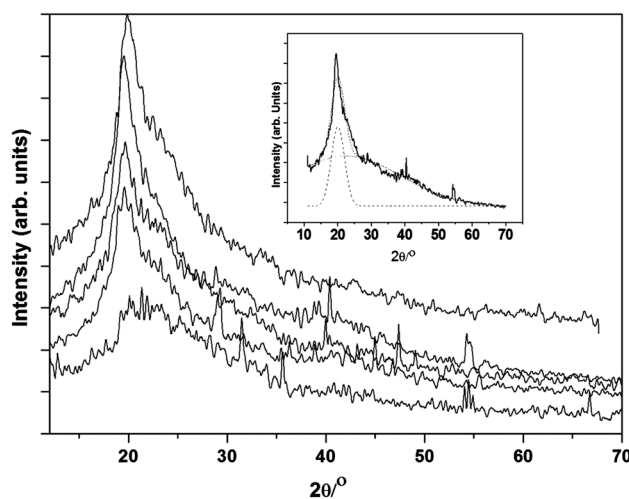


Fig. 5 XRD spectra of PVA and PVA based nanocomposites having 0.2%, 0.4%, 0.8% and 1.0% *f*MWCNTs (bottom to top, respectively). The inset shows the typical fitting for evaluation of relative crystallinity of the nanocomposite film having 0.8% *f*MWCNTs.

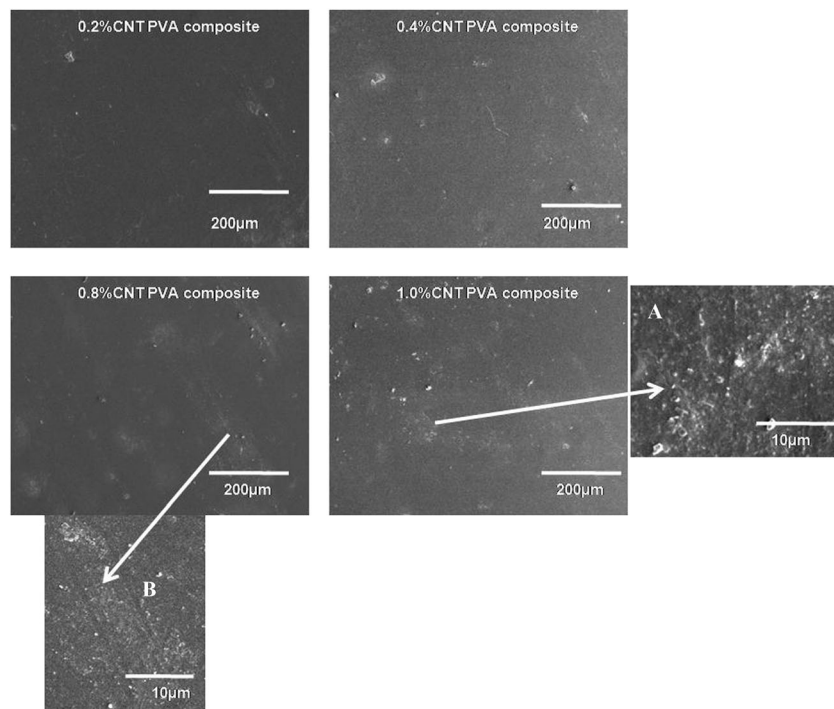


Fig. 6 The SEM images of the surface of the nanocomposite films. Figures (A) and (B) show the magnified image of regions having fMWCNT aggregates.

nanocomposites is probably because PVA chains are restricted from undergoing an ordered arrangement, defined as *molecule movement restriction*, in the presence of fMWCNTs due to available functionalities and mechanical properties of fMWCNTs. The relative crystallinity was observed to be highest for 0.4% loading (27.3%) and decreased further with fMWCNT loading. This indicates that dispersion of fMWCNTs is hampered at higher concentration and aggregates of fMWCNTs can be present at higher loading. The characteristic diffraction peak of MWCNTs in nanocomposites (Fig. 5) could not be seen probably due to its low concentration (maximum loading 1.0%).

In order to observe the dispersion of fMWCNTs, SEM images of the nanocomposite films were taken and are shown in Fig. 6. It is evident that in the case of 0.2% and 0.4% loading, fMWCNTs were uniformly distributed within the PVA matrix offering good interfacial interaction and the individual fMWCNTs preserved their morphology in these cases. Therefore, solution mixing is found to be an efficient method to disperse individual fMWCNTs by enhancing the interfacial adhesion with the PVA matrix. On the other hand, at higher loading (0.8 and 1.0%), aggregates of fMWCNTs are observed in SEM images. This indicates that by the present method about 0.4 wt% fMWCNTs can be efficiently dispersed in the PVA matrix without agglomeration. The enhancement in crystallinity is attributed to the ordered arrangement of PVA chains due to the interaction between PVA molecules and functionalities, -NH_2 in this study, present on the MWCNT surface. To investigate this interaction, FTIR spectra of the nanocomposites were recorded and are shown in Fig. 7. The FTIR spectra of PVA show the characteristic peaks of PVA and no significant changes are observed after incorporation

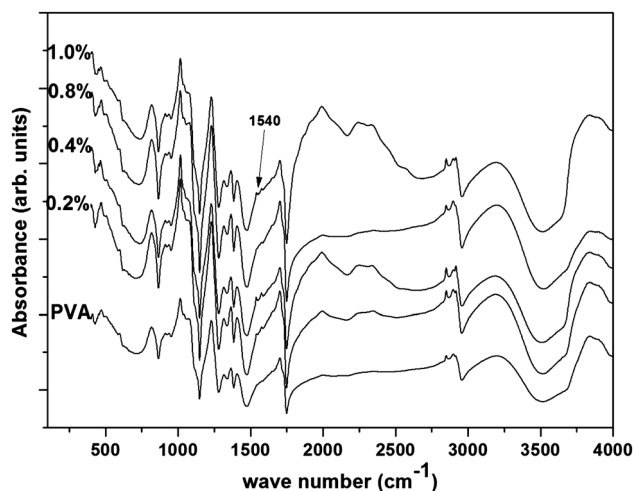


Fig. 7 FTIR spectra of PVA and PVA-fMWCNT composites having 0.2, 0.4, 0.8 and 1.0 wt% fMWCNTs.

of fMWCNTs. However, small changes are observed in terms of broadening of the hump observed at $\sim 3200 \text{ cm}^{-1}$ indicating hydrogen bonding between the -OH group of PVA molecules and the -NH_2 group at the surface of fMWCNTs. An IR peak of low intensity at $\sim 1540 \text{ cm}^{-1}$ (-N-H bending) is also observed for the nanocomposite films confirming the presence of -NH_2 groups in the PVA matrix.

3.3. Positron annihilation spectroscopy and small angle X-ray scattering

It is well known that a distribution of *o*-Ps lifetimes around their mean is observed in the case of disordered (amorphous/

semicrystalline) materials having a size and shape distribution of local free volumes. The program CONTIN is used to fit the PALS spectra to evaluate the distribution of lifetimes.²⁸ In this method, the positron lifetime spectrum $s(t)$ is expressed as the Laplace transformation of the function $\alpha(\lambda)\lambda$. Here, $\alpha(\lambda)$ is the probability density function of the annihilation rate, λ , and is expressed by the Gaussian distribution as given by eqn (2):

$$\alpha_i(\lambda)\lambda d\lambda = \frac{1}{\sigma\sqrt{2\pi}} \exp\left[-\frac{(\ln \lambda/\lambda_{i0})^2}{2\sigma^2}\right] d\lambda \quad (2)$$

The subscript i refers to the i th lifetime component and σ gives the standard deviation of the function. The least square fitting involving the convolution of the resolution function of the spectrometer is carried out to evaluate the parameters of these functions. Using this approach, the lifetime spectrum is given by the following equation:

$$N(t) = I_1 \lambda_1 \exp(-\lambda_1 t) + \sum_{i=2,3} I_i \int_0^\infty \alpha_i(\lambda) \lambda \exp(-\lambda t) d\lambda \quad (3)$$

with $\sum_{i=1,2,3} I_i = 1$

The p -Ps contribution is represented by the subscript 1 which is assumed to show a discrete value for the annihilation rate (lifetime). Thus obtained o -Ps annihilation rate (lifetime) distribution is transformed to nanohole radius (eqn (4)) through eqn (1).

$$n(R) = \frac{2\Delta R}{(R + \Delta R)^2} \left[\cos\left(\frac{2\pi R}{R + \Delta R}\right) - 1 \right] \alpha_3(\lambda) \quad (4)$$

Thus evaluated nanohole radius distribution is shown in Fig. 8. Table 1 shows the average radius $\langle R \rangle$ and fwhm ($w = \sigma\sqrt{2 \ln 2}$) corresponding to the distributions observed in Fig. 8. No o -Ps lifetime component corresponding to o -Ps annihilation from water clusters (o -Ps *pick-off* lifetime in water = 1.8 ns) was

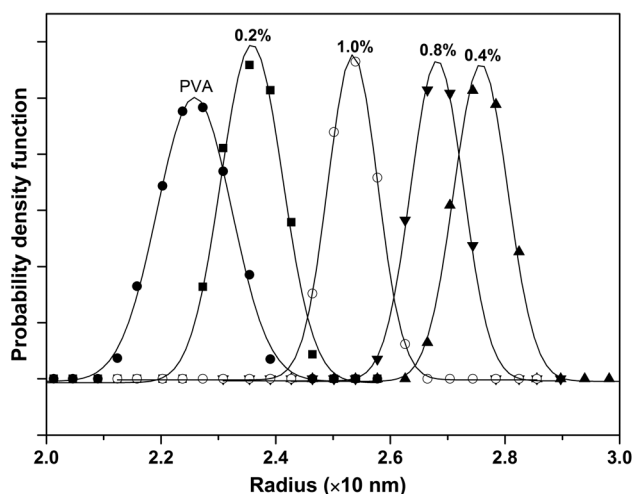


Fig. 8 Distribution of free volume nanoholes in PVA and the nanocomposites. The wt% loading of *f*MWCNTs is mentioned on the peak of the distribution curves.

Table 1 Free volume nanohole radius distribution parameters evaluated from CONTIN analysis^a (Fig. 8)

Quantity Stat. Error	$\langle R \rangle$ (nm) ± 0.002	w (nm) ± 0.001
Pure PVA	2.239	0.152
0.2%	2.339	0.126
0.4%	2.723	0.110
0.8%	2.648	0.108
1.0%	2.512	0.102

^a The evaluated parameters are the result of Gaussian fitting.

observed indicating the absence of water clusters in the samples. On incorporation of *f*MWCNTs, the radius distribution was changed significantly. For example, $\langle R \rangle$ increased from 2.239 nm (pure PVA) to 2.729 nm on 0.4% loading showing a decrease on further loading up to 1.0%. However, the width of distributions showed a continuous decrease in nanohole size distribution (Table 1). Zhou *et al.*²⁹ have reported changes in size distribution on incorporation of MWCNTs in the epoxy matrix. Two peaks were observed in the size distribution where the second one was peaking at higher values compared to the pristine polymer indicating the formation of two regions having different sizes of nanoholes as a result of polymer–MWCNT interactions. In the present case, only one peak was observed in composites at higher values compared to pure PVA. In the case of semicrystalline polymers, the o -Ps lifetime provides information about the nanoholes present in the amorphous region. From FTIR spectra (Fig. 7) it is clear that PVA molecules interact with functionalities available at the *f*MWCNT surface and as a result an ordered arrangement of PVA molecules is formed, which enhances the crystallinity of PVA in nanocomposites as confirmed from XRD measurements (Fig. 5). The changes in o -Ps lifetime or in the nanohole radius show that as a result of interaction between PVA molecules and surface functionalities, the original hydrogen bonded structure of semicrystalline PVA is disrupted producing large size nanoholes with narrower distribution in the amorphous phase. The extent of disruption of the structure mainly depends on the dispersion of *f*MWCNTs. The decrease in o -Ps lifetime beyond 0.4% loading indicates the poor dispersion or aggregation of *f*MWCNTs in the matrix. The aggregation of *f*MWCNTs at higher concentration has been confirmed from SEM images of the nanocomposites (Fig. 6).

In order to obtain more information about the nanoholes present in the nanocomposites, CDB measurements were carried out. These measurements being element sensitive can provide information about the polar groups and the chemical surrounding of nanoholes in semicrystalline systems.^{19,30} Fig. 9 shows the ratio curves of the nanocomposites with respect to pure PVA. The figure shows no significant changes in the ratio curves for 0.2 and 0.4% loading up to $P_L = 20 \times 10^{-3} m_0 c$. However, in the case of nanocomposites with higher loading (0.8 and 1.0%) a significant reduction in the area under momentum region ($5 \times 10^{-3} \langle P_L \rangle 20 \times 10^{-3}$) is observed. In the presence of positronium formation, as in the case of polymer nanocomposites, the momentum density distribution

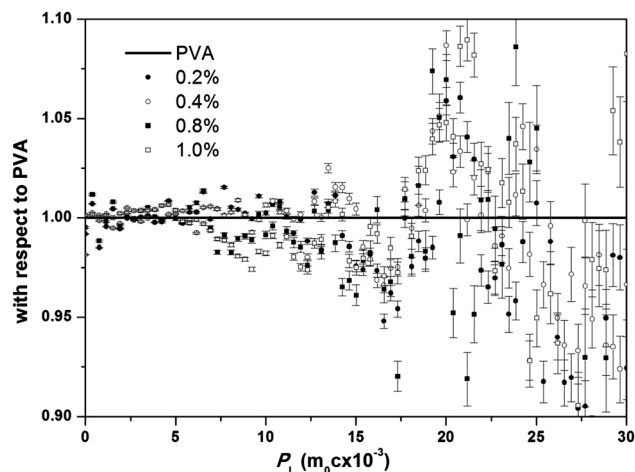


Fig. 9 The CDB ratio curves of PVA based nanocomposites with respect to pure PVA.

(MDD) obtained from these measurements is decomposed into positron and positronium contribution according to the following equation:³¹

$$N(P_L) = (1 - f)N_{Ps}(P_L) + fN_{e^+}(P_L) \quad (5)$$

where $N(P_L)$, $N_{e^+}(P_L)$ and $N_{Ps}(P_L)$ are the experimental MDD, contribution from free positron annihilation and contribution from Ps (*p*-Ps as well as *o*-Ps) annihilation, respectively. It is to be noted that source components have not been deconvoluted in this analysis. The typical deconvolution for pure PVA is shown in the inset of Fig. 10 showing that free positron annihilation primarily contributes beyond $P_L > 5 \times 10^{-3} m_0 c$. Hence, the variation in ratio curves beyond $P_L = 5 \times 10^{-3} m_0 c$, contributed by free positrons, can be indexed to obtain information about the polar groups and the chemical surrounding

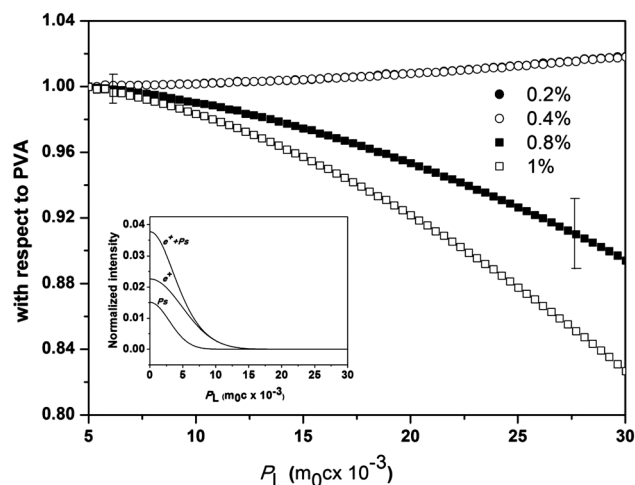


Fig. 10 The CDB ratio curves with respect to PVA obtained for free positron annihilation contribution in the nanocomposites. For the sake of clarity, the average error bars are shown in the lower and higher momentum regions. The inset shows the deconvolution of the momentum density distribution into free positron and positronium contribution for pure PVA.

of nanoholes in PVA based nanocomposites. The ratio curves for free positron contribution for the nanocomposites have been calculated as $N'_{\text{nanocomposite}}(P_L)/N'_{\text{PVA}}(P_L)$, where $N'_{\text{nanocomposite}}(P_L)$ and $N'_{\text{PVA}}(P_L)$ represent the normalized MDD for the nanocomposites and pure PVA in the momentum region ($P_L > 5 \times 10^{-3} m_0 c$), respectively. Thus calculated MDD ratio curves for the nanocomposites are shown in Fig. 10. The ratio curves for nanocomposites having 0.2 and 0.4% fMWCNTs do not show significant changes from PVA indicating similar chemical surrounding of nanoholes. However, the decrease in the area under high momentum region for higher loading (0.8 and 1.0%) indicates the free positron trapping at a different site compared to -OH and -NH₂ groups. The most probable annihilation site is fMWCNT aggregates where free positrons solely annihilate with C atoms having low contribution in the higher momentum region. The presence of fMWCNT aggregates has also been indicated by PALS results and confirmed by SEM.

In order to investigate the volume fraction of the crystalline domains and their size and structure, SAXS measurements were carried out. From Fig. 11, it is evident that SAXS profiles may be divided into two zones. Zone-I contains the information about scattering from fMWCNTs and it is observed that functionality of the scattering profiles changes significantly in zone-I on increasing the concentration of the fMWCNTs. Zone-II of the scattering profiles mainly contains the information about the PVA matrix. The scattering profiles have also been plotted in the form of Kratky plots ($I(q) \times q^2$ vs. q^2) as depicted in Fig. 12. In the present work, the focus is on investigating the changes in the nanostructure of the PVA matrix as a function of fMWCNT concentration. Hence, the changes observed in the SAXS profile in Zone-II were investigated in detail. The isotropic scattering patterns obtained for semicrystalline PVA were modeled using the Hosemann model³² to evaluate the fundamental parameters of the lamellar stacks, namely, the thickness l_c and l_a of the crystalline lamellae and amorphous layers, respectively. The average long period L_p can be simply deduced by $L_p = l_c + l_a$.

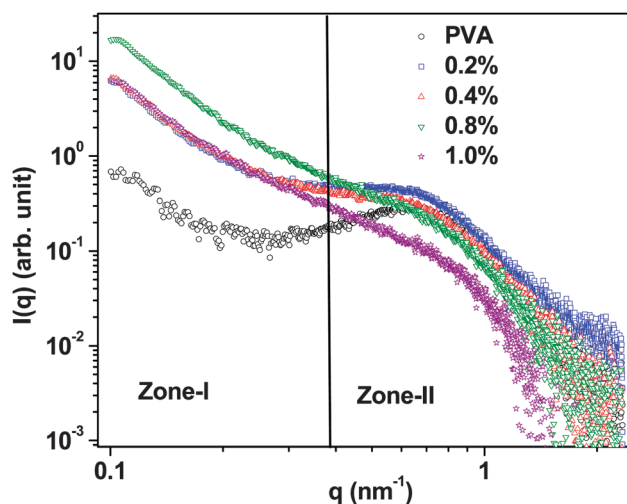


Fig. 11 The SAXS profiles for PVA and PVA based nanocomposites.

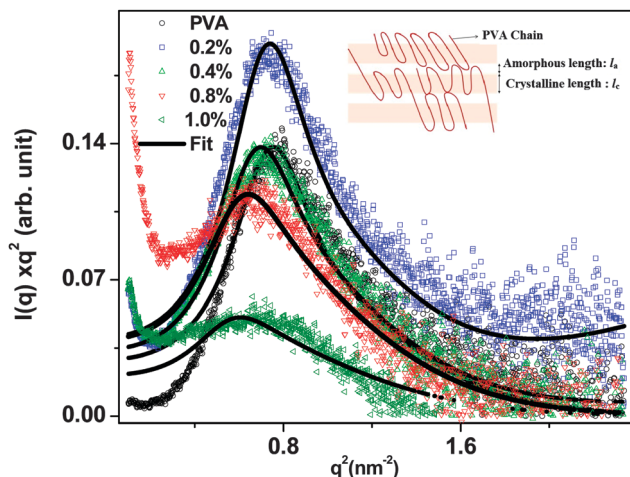


Fig. 12 The SAXS profiles as a Kratky plot ($I(q) \times q^2$ vs. q^2) of PVA and PVA based nanocomposites. The inset shows the schematic of PVA lamellar structure consisting of amorphous and crystalline regions assumed for SAXS analysis.

These quantities can be determined by modeling the lamellar stack structure and obtaining the best fit of a theoretical SAXS intensity distribution, calculated for the assumed model of stacks, to the experimental curve. Generally, for this method, lamellar stacks are characterized by the average thickness of the crystalline lamellae l_c and the amorphous layers l_a and by their independent distribution functions $h_c(z)$ and $h_a(z)$, respectively. To evaluate these parameters, the Kratky plots shown in Fig. 12 were fitted to eqn (6).

$$I(q) = \frac{I_0}{q^4} \exp(-\sigma_{el}^2 q^2) \text{Re} \left[\frac{(1-f_c)(1-f_a)}{(1-f_c f_a)} \right] \quad (6)$$

Here, I_0 is a constant and the exponential term in the numerator accounts for the changes in the SAXS intensity profile caused by a transition layer between crystalline and amorphous regions. The parameter σ_{el} characterizes a sigmoidal electron-density profile in the layer which is assumed to be a Gaussian function. The parameters f_c and f_a are the Fourier transforms of the thickness distribution functions $h_c(z)$ and $h_a(z)$, respectively.

$$f_c(q) = \exp(i l_c q) \exp\left(\frac{-\sigma_c^2 q^2}{2}\right) \quad (7a)$$

$$f_a(q) = \exp(i l_a q) \exp\left(\frac{-\sigma_a^2 q^2}{2}\right) \quad (7b)$$

The extracted parameters estimated from the SAXS analysis are shown in Table 2. It is observed from SAXS measurements

Table 2 The extracted parameters obtained from SAXS analysis using the Hosemann model

Sample	l_c (nm)	σ_c (nm)	l_a (nm)	σ_a (nm)
Pure PVA	5.0	2.5	2.1	0.6
0.2%	5.1	2.6	2.1	0.6
0.4%	5.3	2.9	2.1	0.6
0.8%	5.3	3.5	2.1	0.6
1.0%	5.3	3.9	2.1	0.6

that PVA has the lamellar structure of crystalline and amorphous layers in the nanocomposites. The thickness of crystalline lamellae and the amorphous layer was observed to follow a Gaussian distribution with average length 5.0 and 2.1 nm, respectively. The crystalline thickness of the lamellar polymer structure slightly increases at $>0.4\%$ loading. However, the amorphous thickness distribution remains the same for all the nanocomposites. The results indicate that the nanostructure of PVA at the nm scale does not change significantly on incorporation of fMWCNTs up to 1.0 wt%. However, it is to be noted that significant changes have been observed at the sub-nano level (nanohole size, density and size distribution) structure using a positronium probe even at the lowest studied fMWCNT concentration, *i.e.* 0.2%.

3.4. Thermal and mechanical properties

In order to evaluate the thermal stability of the nanocomposites, TGA measurements under an inert atmosphere were carried out. Fig. 13 (inset) shows the typical TGA curves for pure PVA and the nanocomposite having 1.0% fMWCNTs indicating two weight loss processes. The TGA curves shown in the inset of the figure indicate changes in the rate of decomposition of the PVA matrix. The two weight loss steps are assigned to loss of water and some volatiles due to pyrolyzation, respectively.³³ Fig. 13 (inset) shows that the removal of absorbed water is complete (<450 K) well before the beginning of decomposition of these samples (~ 550 K). Thus, removal of water during TGA will not really hamper the mechanism of decomposition of these samples. Fig. 13 shows the derivative of TGA curves for PVA and the nanocomposites. The presence of two peaks confirms the two-step weight loss mechanism for PVA and the nanocomposites. The second peak, attributed to loss of volatiles, shows a broad hump at higher temperature (~ 710 K) and may be due to the presence of PVA crystallites. To compare the thermal stability of the composites, the second peak in derivative curves has been fitted as a combination of

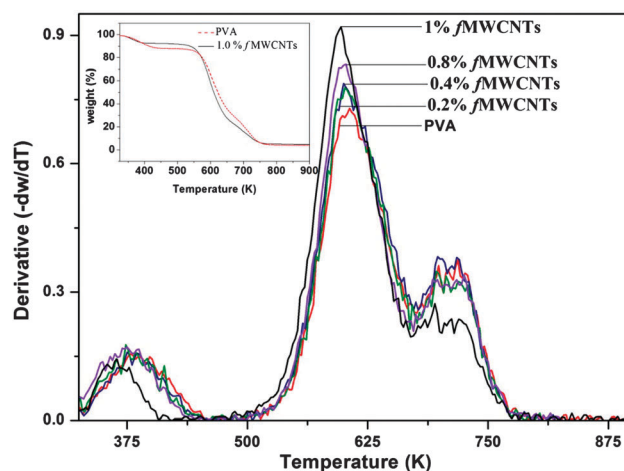


Fig. 13 Derivative of TGA curves of PVA and the nanocomposite films. The inset shows the typical TGA curves obtained for PVA and the nanocomposite with 1.0% fMWCNT loading.

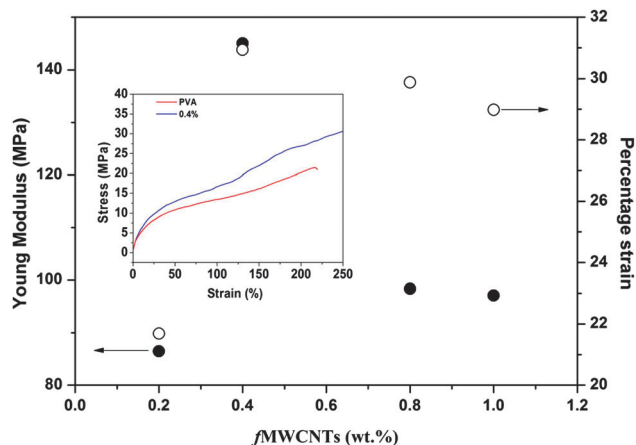


Fig. 14 Young's modulus and percentage strain of the nanocomposite films as a function of *f*MWCNT loading. The inset in the figure shows the typical measurements of stress–strain for pure PVA and 0.4% *f*MWCNT loading.

two Gaussian peaks and the peak position temperatures are taken as temperatures of decomposition ($T_{1,\text{dec}}$ and $T_{2,\text{dec}}$). It was observed that $T_{1,\text{dec}} = 609$ K and $T_{2,\text{dec}} = 710$ K remain the same up to 0.4% loading and decrease to 604, 708 K for 0.8% and 600 and 700 K for 1.0% loading. From this study it is observed that thermal stability does not alter on incorporation of exfoliated *f*MWCNTs in the PVA matrix but on aggregation of *f*MWCNTs thermal stability is deteriorated. Fig. 14 shows the variation of Young's modulus as well as percentage strain vs. *f*MWCNT loading. The observed Young's modulus is of the order of 100 MPa which is lower compared to reported values for PVA in a completely dried state. In the present study, the samples were dried following the same procedure as used before for positron annihilation and SAXS measurements. The PALS measurements indicated the absence of any water clusters in the samples after the heat treatment as discussed earlier. On the other hand, the observed lower value of Young's modulus indicates the presence of water molecules which may be distributed in the matrix without forming water clusters. The presence of these water molecules may lead to lower Young's modulus and higher ductility. In order to exclude the effect of water molecules, the relative change in Young's modulus of the nanocomposite films with PVA was calculated and plotted in Fig. 15. The inset in Fig. 14 shows the typical engineering stress vs. strain measurements for pure PVA and the 0.4% *f*MWCNT loaded sample. It was observed that the nanocomposite film with 0.4% loading shows superior mechanical properties in terms of Young's modulus and percentage strain on elongation (Fig. 14). The observed superior properties at 0.4% loading are the result of enhanced interfacial interaction between PVA and *f*MWCNTs. The improved interfacial interaction results in improved crystallinity as observed from XRD and supported by PALS results. The 0.4% nanocomposites have the largest size of nanoholes as observed from PALS. In general, larger nanoholes are shown to be responsible for poorer mechanical properties of polymers. In the present case, PVA nanocomposites are semicrystalline and the nanoholes measured using PALS are present in the

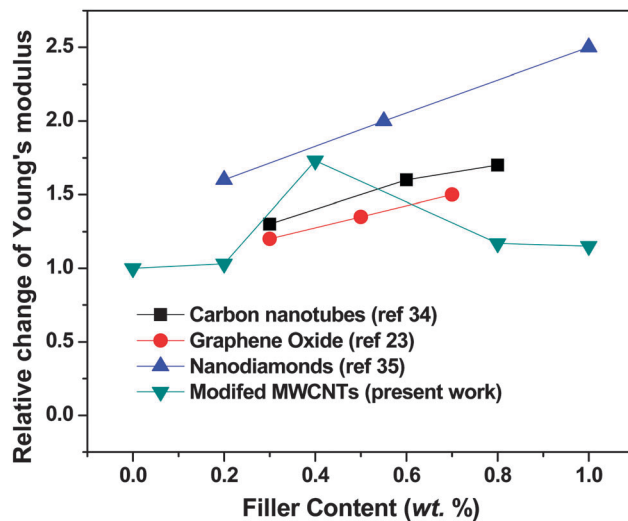


Fig. 15 The relative change of Young's modulus (nanocomposite/PVA) with percentage filler content in the nanocomposite films. (The relative Young's moduli of the graphene oxide, carbon nanotube and nanodiamond filled films were taken from the literature.)

amorphous region. It seems that the mechanical properties of the nanocomposites are primarily governed by the ordering of PVA molecules at the *f*MWCNT surface which enhances the load transfer between PVA molecules and MWCNTs. Fig. 15 shows the relative change of Young's modulus with respect to pure PVA as a function of carbon filler content in the nanocomposite films. It shows that the 0.4% *f*MWCNT–PVA composite has superior strength with respect to unmodified CNT and graphene oxide filled PVA nanocomposites as reported in the literature.^{23,34} In fact the strength of the film was almost equivalent to that of the nanodiamond filled nanocomposite film which has been shown to have superior strength compared to other carbon nanofillers.³⁵ It further confirms that functionalization of MWCNTs really improves the interaction between MWCNTs and the PVA matrix. This improved interaction leads to the ordering of PVA molecules at the *f*MWCNT surface and efficient load transfer takes place between PVA molecules and nanotubes resulting in improvement of mechanical strength.

4. Conclusion

The structure of PVA–*f*MWCNT composites at the sub-nano and nano level has been characterized to explore the correlation of evolved nanostructure with thermal as well as mechanical properties of the nanocomposites. The free volume (sub-nano level) properties, studied using positron annihilation spectroscopy, were observed to change significantly depending on the extent of loading of *f*MWCNTs as well as their dispersion in the PVA matrix. On the other hand, no significant changes were observed in the lamellar structure (nano level) of the PVA matrix as studied using small angle X-ray scattering. The changes observed in the nanostructure are due to variation in the interfacial interaction between PVA molecules and MWCNTs. It is observed that functionalization of MWCNTs

improves the interfacial interaction between PVA molecules and MWCNTs resulting in an ordered arrangement of PVA molecules on the surface of MWCNTs. In such a scenario, efficient load transfer takes place between PVA and MWCNTs resulting in improved mechanical strength of the nanocomposites.

Acknowledgements

The authors are thankful to Mr Bhaskar Paul, Dr Naina Raje and Dr Hemant Sodaye from BARC, India, for their help with SEM, TGA and stress-strain measurements, respectively.

References

- 1 S. Wang, Z. Liang, P. Gonnet, Y.-H. Liao, B. Wang and C. Zhang, *Adv. Funct. Mater.*, 2007, **17**, 87.
- 2 C. Bao, Y. Guo, L. Song and Y. Hu, *J. Mater. Chem.*, 2011, **21**, 13942.
- 3 L. S. Schadler, S. C. Giannaris and P. M. Ajayan, *Appl. Phys. Lett.*, 1998, **73**, 3842.
- 4 Y. Wang, Z. Shi and J. Yin, *J. Phys. Chem. C*, 2010, **114**, 19621.
- 5 A. Rasheed, H. G. Chae, S. Kumar and M. D. Dadmun, *Polymer*, 2006, **47**, 4734.
- 6 L. Ci, J. Suhr, V. Pushparaj, X. Zhang and P. M. Ajayan, *Nano Lett.*, 2008, **8**, 2762.
- 7 A. Koval'chuk, V. G. Shevchenko, A. N. Shchegolikhin, P. M. Nedorezova, A. N. Klyamkina and A. M. Aladyshev, *Macromolecules*, 2008, **41**, 7536.
- 8 W.-L. Song, W. Wang, L. M. Veca, C. Y. Kong, M.-S. Cao, P. Wang, M. Mezziani, J. H. Qian, G. E. LeCroy, L. Cao and Y.-P. Sun, *J. Mater. Chem.*, 2012, **22**, 17133.
- 9 Y. Hou, J. Tang, H. Zhang, C. Qian, Y. Feng and J. Liu, *ACS Nano*, 2009, **3**, 1057.
- 10 M. M. J. Treacy, T. W. Ebbesen and J. M. Gibson, *Nature*, 1996, **381**, 678.
- 11 T. Uchida and S. Kumar, *J. Appl. Polym. Sci.*, 2005, **98**, 985.
- 12 D. H. Walt, *MRS Bull.*, 2004, **29**, 281.
- 13 S. Bhattacharyya, C. Sinturel, J. P. Salvetat and M.-L. Saboungi, *Appl. Phys. Lett.*, 2005, **86**, 113104.
- 14 J. Zhang, M. Yang and F. H. J. Maurer, *Macromolecules*, 2011, **44**, 5711.
- 15 S. Harms, K. Ratzke, F. F. Gerald, J. Schneider, L. Willner and D. Richter, *Macromolecules*, 2010, **43**, 10505.
- 16 R. Zaleski, A. Kierys, M. Grochowicz, M. Dziadosz and J. Goworek, *J. Colloid Interface Sci.*, 2011, **358**, 268.
- 17 S. Awad, H. Chen, G. Chen, X. Gu, J. L. Lee, E. E. Abdel-Hady and Y. C. Jean, *Macromolecules*, 2011, **44**, 29.
- 18 S. K. Sharma, J. Prakash, K. Sudarshan, P. Maheshwari, D. Sathiyamoorthy and P. K. Pujari, *Phys. Chem. Chem. Phys.*, 2012, **14**, 10972.
- 19 S. K. Sharma, J. Bahadur, P. N. Patil, P. Maheshwari, S. Mukherjee, K. Sudarshan, S. Mazumder and P. K. Pujari, *ChemPhysChem*, 2013, **14**, 1055.
- 20 S. J. Tao, *J. Chem. Phys.*, 1972, **56**, 5499.
- 21 M. Eldrup, D. Lightbody and J. N. Sherwood, *Chem. Phys.*, 1981, **63**, 51.
- 22 Y. X. Xu, W. J. Hong, H. Bai, C. Li and G. Q. Shi, *Carbon*, 2009, **47**, 3538.
- 23 J. J. Liang, Y. Huang, L. Zhang, Y. Wang, Y. F. Ma, T. Y. Guo and Y. S. Chen, *Adv. Funct. Mater.*, 2009, **19**, 2297.
- 24 X. Zhao, Q. H. Zhang, D. J. Chen and P. Lu, *Macromolecules*, 2010, **43**, 2357.
- 25 H. J. Salavagione, G. Martinez and M. A. Gomez, *J. Mater. Chem.*, 2009, **19**, 5027.
- 26 C. Branca, F. Frusteri, V. Magazu and A. Mangione, *J. Phys. Chem. B*, 2004, **108**, 3469.
- 27 C. Zhang, S. Huang, W. W. Tjiu, W. Fan and T. Liu, *J. Mater. Chem.*, 2012, **22**, 2427.
- 28 S. W. Provencher, *Comput. Phys. Commun.*, 1982, **27**, 213.
- 29 W. Zhou, J. Wang, G. Zhenli, J. Gong, N. Qi and B. Wang, *Appl. Phys. Lett.*, 2009, **94**, 021904.
- 30 K. Sato, H. Murakami, K. Ito, K. Hirata and Y. Kobayashi, *Radiat. Phys. Chem.*, 2009, **78**, 1085.
- 31 N. Djourellov, C. He, T. Suzuki, V. Shantarovich, Y. Ito, K. Knodo and Y. Ito, *Radiat. Phys. Chem.*, 2003, **68**, 689.
- 32 R. Hosemann and S. N. Bagchi, *Direct Analysis of Diffraction by Matter*, North Holland, Amsterdam, The Netherlands, 1962.
- 33 P. S. Thomas, J.-P. Guerbois, G. F. Russell and B. J. Briscoe, *J. Therm. Anal. Calorim.*, 2001, **64**, 501.
- 34 L. Q. Liu, A. H. Barber, S. Nuriel and H. D. Wagner, *Adv. Funct. Mater.*, 2005, **15**, 975.
- 35 S. Morimune, M. Kotera, T. Nishimo, K. Gota and K. Hata, *Macromolecules*, 2011, **44**, 4415.